

SN 2017hpa: A carbon-rich type Ia supernova

Anirban Dutta^{1*}, Avinash Singh², G. C. Anupama¹, D. K. Sahu¹ and Brajesh Kumar²

¹Indian Institute of Astrophysics, II Block, Koramangala, Bangalore 560 034, India

²Aryabhata Research Institute of Observational Sciences, Manora Peak, Nainital, 263 001 India

Accepted ———, Received ———; in original form ———

ABSTRACT

We present the optical (*UBVRI*) and ultraviolet (*Swift*-*UVOT*) photometry, and optical spectroscopy of Type Ia supernova SN 2017hpa. We study broadband UV+optical light curves and low resolution spectroscopy spanning from -13.8 to $+108$ d from the maximum light in *B*-band. The photometric analysis indicates that SN 2017hpa is a normal type Ia with $\Delta m_B(15) = 0.98 \pm 0.16$ mag and $M_B = -19.45 \pm 0.15$ mag at a distance modulus of $\mu = 34.08 \pm 0.09$ mag. The (*uvw1* – *uvv*) colour evolution shows that SN 2017hpa falls in the NUV-blue group. The (*B* – *V*) colour at maximum is bluer in comparison to normal type Ia supernovae. Spectroscopic analysis shows that the Si II 6355 absorption feature evolves rapidly with a velocity gradient, $\dot{v} = 128 \pm 7$ km s⁻¹ d⁻¹. The pre-maximum phase spectra show prominent C II 6580 Å absorption feature. The C II 6580 Å line velocity measured from the observed spectra is lower than the velocity of Si II 6355 Å, which could be due to a line of sight effect. The synthetic spectral fits to the pre-maximum spectra using *syn++* indicate the presence of a high velocity component in the Si II absorption, in addition to a photospheric component. Fitting the observed spectrum with the spectral synthesis code *TARDIS*, the mass of unburned C in the ejecta is estimated to be $\sim 0.019 M_{\odot}$. The peak bolometric luminosity is $L_{\text{peak}}^{\text{bol}} = 1.43 \times 10^{43}$ erg s⁻¹. The radiation diffusion model fit to the bolometric light curve indicates $0.61 \pm 0.02 M_{\odot}$ of ⁵⁶Ni is synthesized in the explosion.

Key words: supernovae: general - supernovae: individual: SN 2017hpa, galaxies: individual: UGC 3122

1 INTRODUCTION

Type Ia supernovae (SNe Ia) are widely regarded as explosions due to thermonuclear runaway in a white dwarf (WD), most likely carbon-oxygen with a mass close to the Chandrasekhar limit (Hoyle & Fowler 1960). However, specific progenitor systems and mechanisms driving the explosions have not been clearly identified. Two of the most favoured models for the progenitors are the single degenerate (SD) systems, (Nomoto 1982a,b; Arnett 1982; Iben & Tutukov 1984) and the double-degenerate (DD) systems (Iben & Tutukov 1984; Webbink 1984). In the former case, the WD accretes matter from a non-degenerate companion (giant, main-sequence or helium star) in a close binary system, while in the latter case, the explosion is produced by the merger of two white dwarfs (Kromer et al. 2010; Pakmor et al. 2013). The best-studied models so far involve a Chandrasekhar mass WD explosion (Raskin et al. 2009), but recent studies of sub-Chandrasekhar mass models (Sim et al. 2012; Goldstein & Kasen 2018) have been successful in reproducing the peak brightness and light curve widths of the fast-declining SNe Ia.

A reasonably tight correlation between the luminosity at peak and the light curve decline rate has been established for a majority of normal SNe Ia (Phillips 1993, Phillips et al. 1999), with brighter objects having a slower decline rate. This correlation allows the estimation of precise distances to these objects, and hence the measurement

for the expansion rate of the Universe (Riess et al. 1996, 1998a,b; Phillips et al. 1999; Perlmutter et al. 1999).

There exists a spectroscopic classification (Nugent et al. 1995) defined by the ratio of the equivalent widths of the absorption features of Si II at $\lambda 5972$ and $\lambda 6355$. This ratio, R(Si II), is related with the absolute magnitude of the supernova and hence with the decline rate. It acts as a distance independent luminosity indicator. This is interpreted as due to temperature difference and also the variation in the amount of ⁵⁶Ni produced in the supernova explosion. Based on the ratio of the pseudo-equivalent widths (pEW) of Si II $\lambda 5972$ and $\lambda 6355$ features in the spectra near maximum light, SNe Ia can be grouped into core normal (CN), shallow silicon (SS), broadline (BL) and cool (CL) classes (Branch et al. 2006). This indicates inhomogeneities in the compositional structure and temperature difference in SNe Ia.

Benetti et al. (2005) provided a further sub-classification based on the evolution of the expansion velocity, in which the objects fall under three groups: FAINT, High-Velocity Gradient (HVG), and Low-Velocity Gradient (LVG). There are some hints that the HVG objects could result from delayed detonation, while the LVG objects could be due to deflagration (Lentz et al. 2000; Benetti et al. 2005). This spectral diversity can also be explained by considering an asymmetric explosion viewed from different line of sight (Maeda et al. 2010).

In the pre-maximum phase, spectra of SNe Ia consist of overlapping P-Cygni profiles of intermediate-mass elements (IME's) like Si, S, Mg, Ca, and Iron group elements (IGE's) like Fe, Co, Ni. In some cases, carbon and oxygen features are present in the very early

* E-mail: anirban.dutta@iiap.res.in

spectra, which could result from incomplete burning (Parrent et al. 2011; Folatelli et al. 2012; Maguire et al. 2014). The expansion velocity inferred using these features could provide an essential hint to the velocity structure of the outer expanding ejecta. It is not certain as to whether the unburned material is present only in the outer layers or is mixed within the ejecta, and if so, the extent of mixing. The objects with detection of unburned material are of great importance as they can constrain the amount of material that is still unburned and hence the explosion channel. The pure deflagration model (W7) (Nomoto et al. 1984), and the pulsating delayed detonation models (Hoefflich et al. 1995; Dessart et al. 2014a) leave unburned carbon in the ejecta, while the delayed detonation models burn most of the carbon (Khokhlov 1991; Kasen et al. 2009).

Detailed photometric and spectroscopic study of type Ia supernova SN 2017hpa that showed unburned carbon in its early spectrum are presented in this work. The observed properties of SN 2017hpa are compared with those of normal type Ia supernovae, and its explosion parameters are estimated. Supernova SN 2017hpa¹ was discovered by Gagliano et al. (2017) on 2017 October 25, 08:18:16 UT (JD=2458051.84) in the galaxy UGC 3122². A spectrum obtained on 2017 October 25 23:55:02 UT with the Asiago 1.82 m Copernico Telescope equipped with AFOSC was found to be consistent with the very early spectrum of type Ia SN, in particular, SN 1990N ~ 14 days before the maximum light (Floers et al. 2017). Using a spectroscopic redshift of $z = 0.0156$ for the host galaxy, an expansion velocity of $\sim 16,000 \text{ km s}^{-1}$ was deduced from the absorption minimum of Si II $\lambda 6355$. The important parameters of SN 2017hpa and its host galaxy UGC 3122 are presented in Table 1.

Details of the observations and data reduction methods are presented in section 2. The photometric and spectroscopic analysis are discussed in sections 3 and 4, respectively. Finally, we summarise our results in section 5.

2 OBSERVATIONS AND DATA REDUCTIONS

2.1 Optical photometry with 2-m HCT

Bessell *UBVRI* photometric observations of SN 2017hpa were carried out using the Hanle Faint Object Spectrograph Camera (HFOSC), mounted on the 2-m Himalayan Chandra Telescope (HCT) of the Indian Astronomical Observatory (IAO)³, Hanle, India. The HFOSC is equipped with a $2K \times 4K$ SITe CCD chip, and the central $2K \times 2K$ pixels are used for imaging, covering a field of view (FOV) of 10×10 arcmin at an image scale of $0.296 \text{ arcsec pixel}^{-1}$. The readout noise and gain of the camera are $4.87e^-$ and $1.22e^-/\text{ADU}$, respectively. The pre-processing tasks of bias subtraction and flat field correction were performed using the bias and sky flat frames obtained on each night. Cosmic-ray events were removed. All tasks were performed using the standard packages available with *IRAF*. Whenever multiple frames were observed in the same band, they were combined before performing photometry.

For calibrating a sequence of secondary stars in the SN field, photometric standard stars from the list of Landolt (Landolt 1992) were observed along with the SN field on photometric nights. Standard field PG0231+051 was observed on 2017 November 22 and 2018 January 5, while the field PG0918+029 was observed on 2017 December 29. The magnitudes of the standard stars in the Landolt field

and the stars in the SN field were estimated using aperture photometry within the DAOPHOT (Stetson 1987) task in *IRAF*. The average atmospheric extinction coefficients for the site, in each of the passbands *U, B, V, R, I* were adopted from Stalin et al. (2008) and secondary stars in the field were calibrated as mentioned in Singh et al. (2018). Fig. 1 shows the field of SN 2017hpa with the secondary standards identified. The *UBVRI* magnitudes of the local standard stars are listed in Table A1.

The apparent magnitudes of the secondary standard stars were obtained by performing point-spread function (PSF) photometry. The zero points for each night were estimated using the average colour terms for the telescope-detector system. Though the SN lies in the outskirts of its host galaxy, there is a possibility of SN flux contamination from the host and a nearby field star (see Fig. 1). Therefore, to remove any possible contamination and estimate the supernova brightness accurately, template subtraction methodology was adopted. The template images of SN 2017hpa were obtained on 2019 September 23 under good seeing conditions with the 2-m HCT. The templates were astrometrically aligned with the science images (containing the SN), background subtracted, PSF matched, and scaled. The scaled template was then subtracted from the science images, leaving only the supernova in the resultant images. Aperture photometry of the supernova was then performed, and the supernova magnitudes were calibrated using the nightly zero points. Final (template subtracted) SN magnitudes are listed in Table A3 and used for further analysis in the paper.

2.2 UV-Optical Photometry with *Swift* – *UVOT*

SN 2017hpa was also observed with the *Ultra Violet Optical Telescope* (*UVOT*) onboard the Neil Gehrels *Swift* Observatory. The data were obtained from the *Swift* archive (https://www.swift.ac.uk/swift_portal/). The *UVOT* observations were made with broadband filters *uvw2* (1928 Å), *uvm2* (2246 Å), *uvw1* (2600 Å), *u* (3465 Å), *b* (4392 Å) and *v* (5468 Å) starting from 2017 October 26 (JD 2458053.2) and continued till 2017 December 07 (JD 2458095.4). The data reduction was performed using various packages available with HEASOFT (High Energy Astrophysics Software, version 6.27) and with the latest calibration database for the *UVOT* instrument, following the methods as described in Poole et al. (2008) and Brown et al. (2009). The SN was not detected in the *uvw2* and *uvm2* band with considerable signal-to-noise. The supernova magnitude was extracted using UVOTSOURCE task with an aperture size of $5''$ for the source and a similar aperture size to extract the background counts. The final *UVOT* magnitudes are obtained in the Vega system and tabulated in Table A2.

2.3 Spectroscopy

The spectroscopic monitoring of SN 2017hpa with the HCT started on 2017 October 30 (JD 2458057.4) and continued till 2018 February 25 (JD 2458175.1). Low resolution spectra were obtained using grisms, Gr7 (3500-7800 Å) and Gr8 (5200-9100 Å) available with the HFOSC. The log of spectroscopic observations is provided in Table A4. The two-dimensional images were pre-processed in a standard way. One-dimensional spectra were optimally extracted (Horne 1986) from the processed two-dimensional images using the TWODSPEC package in *IRAF*. Arc lamp spectra FeAr and FeNe were used for wavelength calibration. Night sky emission lines were used to check the wavelength calibration, and whenever necessary, small shifts were applied. The wavelength calibrated spectra were

¹ <https://wis-tns.weizmann.ac.il/object/2017hpa>

² <http://leda.univ-lyon1.fr/>

³ https://www.iap.res.in/?q=telescope_iao

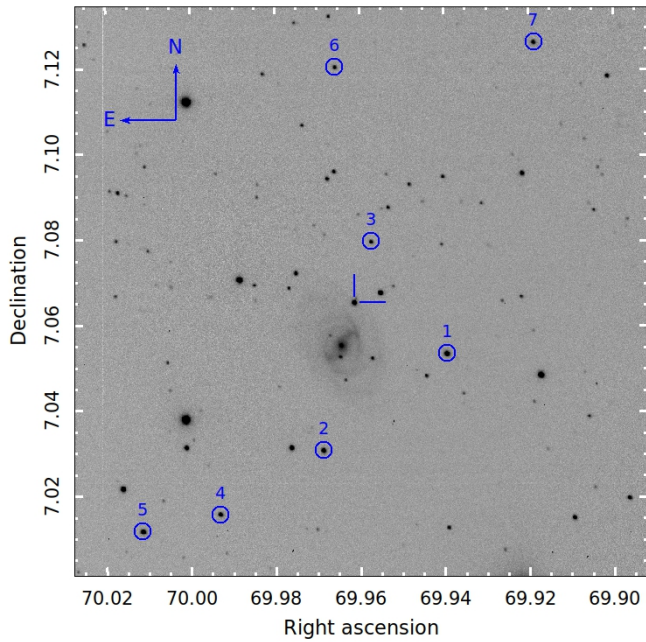


Figure 1. SN 2017hpa in the host galaxy UGC 3122. This is a $\sim 7 \times 7$ arcmin² image in V-band (50 sec exposure) taken with HCT on 2017 October 31. The stars circled in blue (Ids 1–7) are the secondary standard stars used for calibration. The supernova is marked with crosshairs.

corrected for the instrumental response using spectra of spectrophotometric standards and brought to a relative flux scale. On the nights when spectrophotometric standards were not observed, response curves from adjacent nights were used. The flux calibrated spectra in the two grisms were combined, scaled to a weighted mean, to give the final spectrum on a relative flux scale. Finally, the combined spectra were scaled with the broadband *UBVRI* magnitudes to bring it to an absolute flux scale. The spectra have been corrected for redshift ($z = 0.0156$). Telluric features have been removed from the spectra by using the *telluric* package in IRAF.

3 LIGHT CURVE

3.1 Light Curve Analysis

The light curves of SN 2017hpa in *U*, *B*, *V*, *R*, *I*, and *uvw1*, *uvu*, *uvv*, and *uvb* bands are plotted in Fig. 2. The light curve in *U*, *B*, *V*, *R* and *I* bands were fit with MLCS2k2 (Jha et al. 2007) (details of fit provided in Sec. 3.2). The light curve parameters, e.g., the decline rate parameter ($\Delta m_{15}(B)$), time of maximum, and the magnitude at maximum have been calculated from the fitted model, and the associated errors are the observed error propagated with the model error. The *B* band peak magnitude is 15.48 ± 0.11 mag, and $\Delta m_{15}(B) = 0.98 \pm 0.15$ mag. The *I* band light curve shows a distinct secondary peak characteristic of normal SNe Ia. An inflation is also seen in the *R* band light curve around the same epoch. The maximum in the *U* and *I* band light curve occurs at 2.03 d and 3.04 d before *B* band maximum, respectively, and that of *V* and *R* band occurs around ~ 1.02 day after *B* band maximum. The early occurrence of the *I*-band maximum is consistent with other well-observed SNe Ia (Phillips et al. 1999; Anupama et al. 2005). The secondary maximum in the *I*-band light curve occurred at +30.46 d after the *B* band maximum, with a magnitude 0.44 mag fainter than the peak. The double-peaked nature is directly related to the ionisation evolution of Iron Group El-

Table 1. Parameters of SN2017hpa and its host galaxy.

Parameters	Value	Ref.
<i>SN2017hpa:</i>		
RA (J2000)	$\alpha = 04^{\text{h}}39^{\text{m}}50^{\text{s}}.73$	2
DEC (J2000)	$\delta = +07^{\circ}03'55''.22$	2
Galactocentric Location	11'2 W, 35'6 N	2
Discovery Date	$t_d = 2017$ October 25 08:18 (UTC) (JD 2458051.84)	2
Date of <i>B</i> -band Maxima	$t_0 = 2017$ November 08 17:45 (UTC) (JD 2458066.29 \pm 0.11)	1
$\Delta m_{15}(B)$	0.98 ± 0.16 mag	1
Galaxy reddening	$E(B - V) = 0.1518 \pm 0.0069$ mag	3
Host reddening	$E(B - V) = 0.08 \pm 0.06$ mag	1
$(B - V)_0$	-0.26 ± 0.03	1
Peak Magnitude (<i>B</i> -band)	$M_B = -19.45 \pm 0.15$ mag	1
Distance modulus	$\mu = 34.08 \pm 0.09$ mag	1
Peak Luminosity	$L_{\text{peak}}^{\text{bol}} = 1.43 \times 10^{43}$ erg s ⁻¹	1
⁵⁶ Ni mass	$M_{\text{Ni}} = 0.61 \pm 0.02 M_{\odot}$	
Ejected mass	$M_{\text{ej}} = 1.10 \pm 0.22 M_{\odot}$	
\dot{v}	127.9 ± 6.1 km s ⁻¹ d ⁻¹	1
$R(\text{Si II})_{\text{max}}$	0.13 ± 0.02	1
v_{max}	9643 ± 110 km s ⁻¹	1
v_{10}	8320 ± 120 km s ⁻¹	1
Kinetic energy	$E_K = (0.80 \pm 0.23) \times 10^{51}$ erg s ⁻¹	1
<i>UGC 3122:</i>		
Alternate name	MCG+01-12-013, PGC15760, MCG1-12-013, CGCG419-21	4
Type	SBc	4
RA (J2000)	$\alpha = 04^{\text{h}}39^{\text{m}}51^{\text{s}}.50$	4
DEC (J2000)	$\delta = +07^{\circ}03'19''.0$	4
Red-shift	$z = 0.015647 \pm 0.000027$	4

(1) This paper; (2) Gagliano et al. (2017) (3) Schlafly & Finkbeiner (2011) (4) Skrutskie et al. (2006)

ements (IGE's) in the supernova ejecta, (Kasen 2006). As the ejecta expands, it cools down, and at a temperature $T \sim 7000$ K, the near-infrared emission of Fe/Co increases, which marks the transition from doubly to singly ionised state. The appearance of *U* band maximum before and *V* and *R* band maxima after the *B* band maximum is consistent with the model of an expanding cooling atmosphere. However, the appearance of *I* band maximum before *B* band is in sharp contrast to the simple thermal model (Contardo et al. 2000).

In Fig. 3, the *UBVRI* light curves of SN 2017hpa have been compared with other well studied SN Ia, like SN 1990N, SN 1991T (Lira et al. 1998), SN 2003du (Anupama et al. 2005; Stanishev et al. 2007), SN 2005cf (Wang et al. 2009a), SN 2011fe (Vinkó et al. 2012), SN 2012fr (Zhang et al. 2014), SN 2017cbv (Hosseinzadeh et al. 2017; Wee et al. 2018) and SN 2018oh (Li et al. 2019). All the light curves have been shifted to match with their respective *B* band maximum and to their peak magnitudes. It is evident from Fig. 3 that the light curves of SN 2017hpa are similar to normal SNe Ia. The decline rate of the light curves has been calculated by a least-square fit to the data around 30–80 days after *B* band maximum, and the decline rate is given in units of mag (100 d)⁻¹. The decline rate in *B* and *I* bands are estimated as 2.03 ± 0.01 and 4.48 ± 0.01 , respectively.

The reddening corrected (*uvw1* – *uvv*), (*U* – *B*), (*B* – *V*), (*V* – *R*)

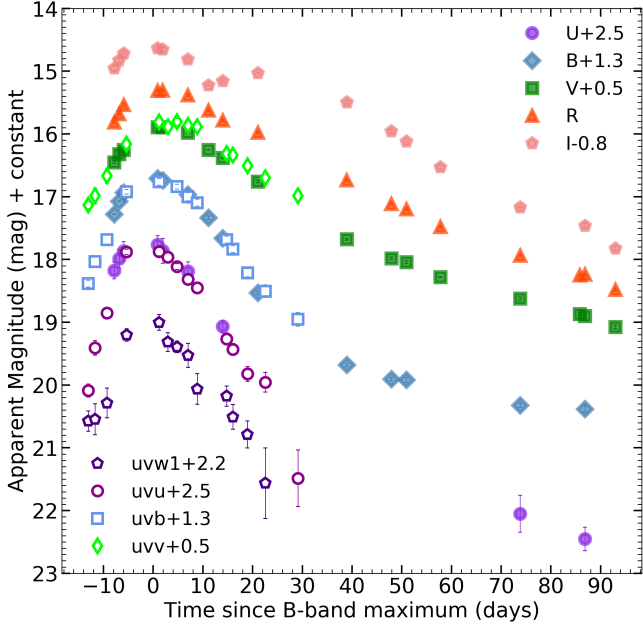


Figure 2. *UBVR* and *Swift-UVOT* light curves of SN 2017hpa. The phase is measured with respect to *B* band maximum. The light curves in individual bands have been shifted for representation purpose as indicated in the legend.

and $(R - I)$ colour curves of SN 2017hpa is displayed in Fig. 4 and compared with well-studied events. All the SNe have been corrected for reddening due to Milky Way and host, as mentioned in the respective studies. The reddening correction for SN 2017hpa is discussed in Section 3.2. The $(B - V)$ colour at *B*-band maximum is -0.26 ± 0.03 mag, which is bluer than the comparison SNe. The $(uvw1 - uvv)$ colour of SN 2017hpa is bluer, similar to the other NUV-blue objects (see Fig. 4) and hence can be included in the NUV-blue group as defined by Milne et al. (2013). However, the $(uvw2 - uvv)$ colour evolution could not be verified. Recent studies of carbon positive SNe have shown bluer near UV colours (Thomas et al. 2011b; Silverman & Filippenko 2012; Milne et al. 2013), which could be due to unburned carbon present during pre-maximum phases. The $(U - B)$ colour at maximum is slightly redder owing to the absorption by IGE’s at shorter wavelengths. This kind of trend has also been seen in SN 2018oh (Li et al. 2019). The $(V - R)$ colour at maximum is -0.02 ± 0.01 mag. The $(V - R)$ colour is redder than the comparison SNe around 10 to 20 d past maximum, and it follows the same trend as other SNe in the late phase. The $(R - I)$ colour at maximum is -0.24 ± 0.01 mag. The main photometric parameters for SN 2017hpa are listed in Table 2.

3.2 Extinction and Distance Modulus

The dust map of Schlafly & Finkbeiner (2011) gives a colour excess of $E(B - V) = 0.1518 \pm 0.0069$ along the direction of SN 2017hpa due to the ISM within the Milky Way. The reddening of the supernova within the host galaxy can be estimated using various empirical relations.

Turatto et al. (2003) and Poznanski et al. (2012) have shown that the reddening within the host is correlated with the equivalent width of Na I D. We do not detect Na I D absorption feature in our low-resolution spectra near maximum light at the redshift of the host galaxy. This indicates minimal reddening within the host. The Phillips-Lira relation (Phillips et al. 1999), which uses the $(B - V)$

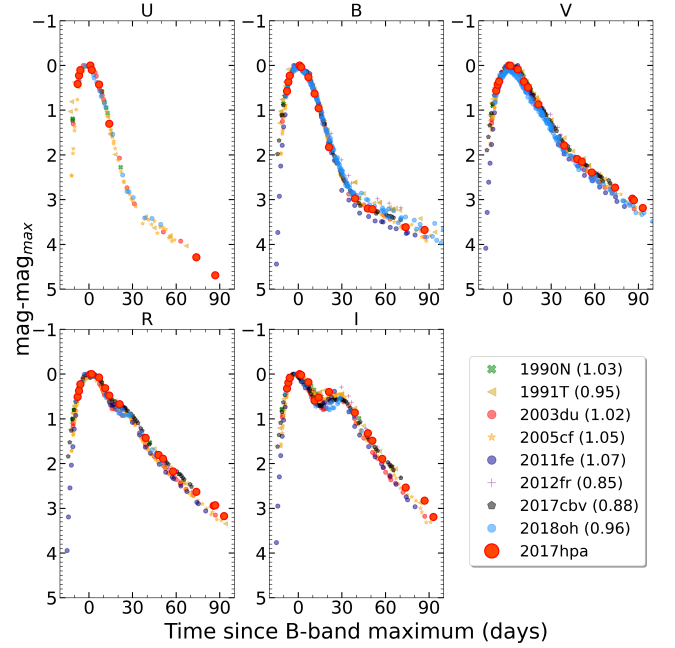


Figure 3. *UBVR* light curves of SN 2017hpa compared with other normal SN Ia. The light curves have been shifted to match with their peak magnitudes and to the epoch of *B* maximum.

colour evolution during 30 to 90 days with respect to the *V*-band maximum, can be used to estimate host reddening. After correcting the $(B - V)$ colour curve for reddening in the Milky-Way, the $(B - V)$ colour curve of SN 2017hpa matches well with the colour predicted by Lira relation if it is shifted by a value of 0.08 ± 0.06 mag. After including the intrinsic dispersion of the Lira relation of ~ 0.05 mag in quadrature, the reddening estimated from the tail of the $(B - V)$ colour evolution $E(B - V)_{\text{tail}}$ is 0.08 ± 0.08 mag. Note the large scatter in the value, which is due to the difference in the slope of the observed $(B - V)$ with the Lira relation. Phillips et al. (1999) also used $B_{\text{max}} - V_{\text{max}}$ color index to estimate $E(B - V)_{\text{host}}$. We estimate $E(B - V)_{\text{max}}$ to be 0.06 ± 0.05 mag. We take an average of $E(B - V)_{\text{tail}}$ and $E(B - V)_{\text{max}}$ to get an estimate of $E(B - V)_{\text{host}}$ to be 0.07 ± 0.09 mag using the $(B - V)$ colours, a value not significantly different from zero.

We have used light curve fitting method MLCS2k2⁴ to estimate the host reddening and distance modulus, and SALT2 to confirm it. We applied the updated version of MLCS2k2 (Riess et al. 1995; Jha et al. 2007) in which the calibration was improved by applying on a sample on 133 SNe Ia for training and extending the model by incorporating *U* band data. In this version, the observed LC of a SN Ia in each passband *X* can be expressed as follows,

$$\vec{m}_X(t - t_0) = \vec{M}_X^0 + \mu_0 + \vec{\zeta}_X(\alpha_X + \frac{\beta_X}{R_V})A_V^0 + \vec{P}_X\Delta + \vec{Q}_X\Delta^2, \quad (1)$$

where t_0 is the epoch of maximum light in *B*-band, \vec{M}_X^0 is the absolute magnitudes of the fiducial SN, μ_0 is the true distance modulus, R_V and A_V^0 are the host galaxy extinction parameters, Δ is the luminosity/light curve shape parameter, and \vec{P}_X and \vec{Q}_X are the vectors describing the change in light curve shape as a quadratic function of Δ . The arrowed quantities span the SN rest frame phase.

⁴ <https://www.physics.rutgers.edu/~saurabh/mlcs2k2/>

Table 2. Photometric parameters of SN 2017hpa.

Filter	JD (Max)	m_{λ}^{\max}	M_{λ}^{\max}	$\Delta m_{15}(\lambda)$	Decline rate* (30–80 d)	Colours at B max
U	2458064.26	15.11 ± 0.13	-19.97 ± 0.18	1.26 ± 0.18	2.332 ± 0.005	–
B	2458066.29	15.48 ± 0.11	-19.45 ± 0.15	0.98 ± 0.16	2.026 ± 0.007	–
V	2458067.31	15.35 ± 0.09	-19.34 ± 0.13	0.59 ± 0.13	3.155 ± 0.005	$(B - V)_0 = -0.26 \pm 0.03$
R	2458067.31	15.24 ± 0.08	-19.31 ± 0.13	0.67 ± 0.12	3.605 ± 0.004	$(V - R)_0 = -0.02 \pm 0.01$
I	2458063.25	15.36 ± 0.07	-19.05 ± 0.13	0.62 ± 0.12	4.483 ± 0.005	$(R - I)_0 = -0.24 \pm 0.01$

*in unit of mag $(100 \text{ d})^{-1}$ and epoch is relative to B band maximum.

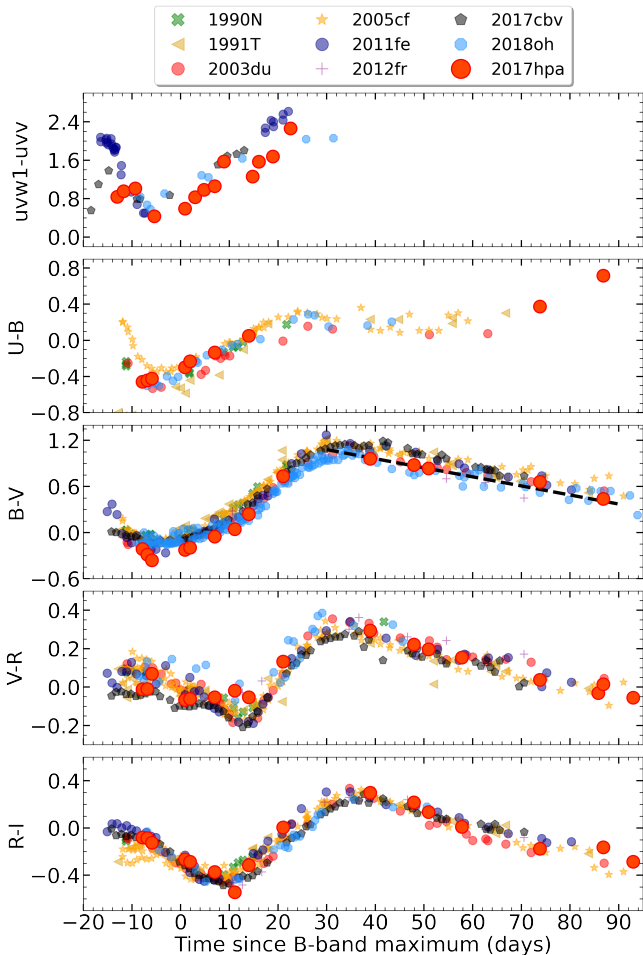


Figure 4. $uvw1 - uvv$, $U - B$, $B - V$, $V - R$ and $R - I$ colour curves of SN 2017hpa plotted along with other well studied SNe Ia. Plotted as black dotted line in the $(B - V)$ colour panel is the Lira relation which has been used to get an estimate of host $E(B - V)$.

We fit our observed $UBVRI$ data with MLCS2k2 and kept the ratio of total-to-selective extinction R_V to be fixed at the Galactic value of 3.1. With this value of R_V we get an extinction A_V^0 of 0.25 ± 0.09 and a distance modulus μ of 33.99 ± 0.06 . In their study of 185 SNe Ia in the CfA3 sample, Hicken et al. (2009) indicate that the Galactic R_V leads to an overestimate of the host extinction, while R_V of 1.7 based on their MLCS2k2 fits provides a more realistic extinction estimate. Recent studies have also indicated a non-Milky Way extinction law for the hosts of SNe Ia. For example, an R_V of 1.7 was estimated for SN 2017cfd (Han et al. 2020), and an R_V of 2.0

was used for the host of SN 2017cbv and SN 2013aa (Burns et al. 2020). Hence, we proceeded with the fit again, keeping R_V as a fit parameter, which resulted in a lower value of $R_V = 1.9$ for the host galaxy and the lowest χ^2 for the fit. The change in the value of R_V has a negligible effect on the distance when the extinction is low because, for such low reddening it is not possible to separate the effect of R_V on the colour of the SN from the intrinsic colour differences between the observed SN and the template. Fig. 5a shows the best fit MLCS2k2 templates to the observed data. With this fit we estimate a distance modulus of 34.07 ± 0.06 mag, and using Fitzpatrick (1999) extinction law, the absolute magnitude in B -band is -19.45 ± 0.15 mag. The estimate of $E(B - V) = 0.08$ matches well with the value estimated based on the observed $(B - V)$ colours at maximum.

We further fit the light curve with Spectral Adaptive Light Curve template (SALT2⁵), which models the spectral energy distribution of SN Ia as:

$$F_{\text{SN}}(p, \lambda) = x_0(M_0(p, \lambda) + x_1 M_1(p, \lambda)) \exp(c C_L(\lambda)), \quad (2)$$

where, F_{SN} is the phase-dependent flux density in the rest-frame of the SN, $p = t - t_0$ is the phase of the SN, x_0 , x_1 , and c are the normalisation, shape, and colour parameter respectively. M_0 , M_1 and C_L are the mean spectral sequence, first-order deviation around the mean sequence and time-independent colour law. These are the trained vectors of SALT2. We applied the SALT2 model (Betoule et al. 2014) with the Landolt-Bessell filter set and used the Vega magnitude system. We used only the observed $UBVRI$ data in the fit. The best-fit templates to the observed data are shown in Fig. 5b.

SALT2 does not fit the distance as a parameter. We therefore calculated the distance modulus using the following relation:

$$\mu_0 = m_B^* - M_B + \alpha x_1 - \beta c, \quad (3)$$

where, m_B^* , x_1 and c are the fit parameters from SALT2 and M_B , α and β are parameters for the distance estimate. We used the values of M_B , α and β from Betoule et al. (2014). The M_B parameter used in the calibration is valid for SNe which exploded in galaxies having total stellar mass $M_{\text{stellar}} \leq 10^{10} M_{\odot}$. For a more massive host galaxy, a correction of -0.061 has to be added to M_B .

As the value of H_0 adopted in MLCS2k2 and SALT2 is $65 \text{ km s}^{-1} \text{ Mpc}^{-1}$ and $68 \text{ km s}^{-1} \text{ Mpc}^{-1}$, respectively we have converted them to $H_0 = 73 \text{ km s}^{-1} \text{ Mpc}^{-1}$ by using the following equation:

$$\mu_0(H_0) = \mu_0(\text{Model}) - 5 \log_{10}(H_0/H_0^{\text{Model}}) \text{ mag}, \quad (4)$$

⁵ <http://supernovae.in2p3.fr/salt/doku.php>

Table 3. Best-fit parameters of the light curve for 2017hpa.

Parameter	Value	Error
MLCS2k2 <i>UBVRI</i>		
R_V	1.9	
T_{max} (MJD)	58066.29	0.11
A_V^{host} (mag)	0.16	0.06
Δ (mag)	-0.17	0.03
μ_0 ($H_0=73$) (mag)	34.07	0.05
χ^2/dof	0.78	
SALT2.4 <i>UBVRI</i>		
T_{max} (MJD)	58066.89	0.06
c	-0.07	0.03
x_0	0.02	0.00
x_1	0.19	0.07
m_B^* (mag)	14.84	0.03
μ_0 ($H_0=73$) (mag)	34.09	0.08
χ^2/dof	2.67	

where "Model" refers to MLCS2k2/SALT2. From SALT2 fit we get a distance modulus of 34.09 ± 0.08 mag. The distance modulus is 34.15 ± 0.08 for a host galaxy of stellar mass $\geq 10^{10} M_\odot$. The main parameters of both the model fits are listed in Table 3.

Throughout the entire analysis, we have used an $R_V = 3.1$ for the Milky Way and an $R_V = 1.9$ for the host galaxy obtained from MLCS2k2 fit. The $E(B - V)$ used for the host is 0.08 ± 0.06 mag. The distance modulus of 34.08 ± 0.09 mag of the SN is obtained by averaging the values from SALT2 and MLCS2k2 fits, assuming the host galaxy stellar mass is $\leq 10^{10} M_\odot$.

3.3 Estimation of Nickel Mass

The bolometric light curve, constructed using the U, B, V, R, I and $uvw1$ magnitudes, is shown in Fig. 6. The apparent magnitudes were corrected for Milky-Way reddening of $E(B - V) = 0.1518 \pm 0.0069$ with $R_V = 3.1$ and a host galaxy reddening of $E(B - V) = 0.08 \pm 0.06$ with $R_V = 1.9$. The reddening corrected magnitudes were converted to flux using zero-points from [Bessell et al. \(1998\)](#). Magnitudes in U, B, V, R and I have been interpolated from MLCS2k2 model light curve and Swift-*UVOT* band has been interpolated by fitting a cubic spline. Then, the spectral energy distribution (SED) is constructed by using the fluxes in *UBVRI* and *UVOT*. A spline curve has been fit to the SED and the area under the curve has been calculated by trapezoidal rule, integrating from 2500–9500 Å. The NIR (9500–24000 Å) flux contribution has been estimated from [Wang et al. \(2009a\)](#) and added to the uv-optical flux. The total flux thus obtained has been converted to luminosity adopting a distance modulus of 34.08. The maximum of the bolometric light curve for SN 2017hpa is $L_{peak}^{bol} = 1.43 \times 10^{43}$ erg s⁻¹. To estimate nickel mass, ejecta mass and other physical parameters of the explosion, we applied the modified radiation diffusion model ([Arnett 1982](#); [Valenti et al. 2008](#); [Chatzopoulos et al. 2012](#)). The model assumes homologously expanding ejecta, spherical symmetric distribution of ejecta material, no mixing, constant optical opacity, small initial radius ($R_0 \sim 0$) and the diffusion approximation for photons. To fit the model we used a Markov-Chain Monte Carlo method. We used the *emcee* package in *python* and optimized the parameters and sampled the posterior

distribution following the methods as described in [Foreman-Mackey et al. \(2013b\)](#). The fit parameters of the model are t_0 - the rise time to maximum since the day of explosion, M_{Ni} - the initial ⁵⁶Ni mass produced, t_{lc} - the light curve time scale and t_γ - the gamma-ray leaking time scale. The fit to the bolometric light curve gives a rise time to maximum $t_0 = 16.93 \pm 0.23$ days, $t_{lc} = 13.38 \pm 0.47$ days, $t_\gamma = 41.4 \pm 0.8$ days and $M_{Ni} = 0.61 \pm 0.02 M_\odot$.

The ejected mass (M_{ej}) and the expansion velocity (v_{exp}) are related to the two timescale parameters t_{lc} and t_γ of the radiation model by

$$t_{lc}^2 = \frac{2\kappa M_{ej}}{\beta c v_{exp}} \text{ and } t_\gamma^2 = \frac{3\kappa_\gamma M_{ej}}{4\pi v_{exp}^2}. \quad (5)$$

Here, κ is the effective optical opacity, $\kappa_\gamma = 0.03$ cm² g⁻¹ is the opacity for γ -rays ([Clocchiatti & Wheeler 1997](#); [Wheeler et al. 2015](#)), and $\beta = 13.8$ is a constant of integration [Arnett \(1982\)](#). These two equations can be used to constrain three parameters of explosion, M_{ej} , v_{exp} and κ . Following ([Li et al. 2019](#)) and ([Könyves-Tóth et al. 2020](#)), we can get a lower bound on κ assuming $M_{ej} \leq M_{Ch}$, while the upper limit on κ is obtained assuming v_{exp} has a lower limit of 9500 km s⁻¹, estimated from the Si II $\lambda 6355$ absorption feature near maximum light. In this way, the limits of κ , i.e. $\kappa_{lower} = 0.12 \pm 0.01$ cm² g⁻¹ and $\kappa_{upper} = 0.16 \pm 0.01$ cm² g⁻¹, are estimated, and the effective optical opacity is taken to be $\kappa = 0.14 \pm 0.01$. Finally, by using the equations

$$M_{ej} = \frac{3\kappa_\gamma t_{lc}^4 \beta^2 c^2}{16\pi t_\gamma^2 \kappa^2}; v_{exp} = \frac{3\kappa_\gamma t_{lc}^2 \beta c}{8\pi \kappa t_\gamma^2} \text{ and } E_{kinetic} = 0.3 M_{ej} v_{exp}^2, \quad (6)$$

we estimate $M_{ej} = 1.10 \pm 0.22 M_\odot$, $v_{exp} = 11,060 \pm 1200$ km s⁻¹ and kinetic energy $E_{kinetic} = 0.80 \pm 0.23 \times 10^{51}$ erg.

4 SPECTRAL ANALYSIS

The spectra of SN 2017hpa were obtained from days -8.9 to +108 since the B -band maximum. In our analysis, we have also used the earliest spectrum available for SN 2017hpa in WISereP ([Yaron & Gal-Yam 2012](#)),⁶ taken at -13.8 d with the Asiago Faint Object Spectrograph and Camera (AFOSC). All spectra were corrected for a redshift of 0.015 and a reddening value of $E(B - V) = 0.15$ mag for the Milky Way and $E(B - V) = 0.08$ mag for the host galaxy. The spectroscopic features have been identified by comparing with other SNe Ia around similar phases.

4.1 Pre-maximum phase

The pre-maximum spectra during -13.8 to -5.9 d are plotted in Fig 7. The spectra show blue continuum with prominent absorption due to Ca II H & K ($\lambda 3934, 3968$), Fe III, Mg II, Si III and Si II ($\lambda 6355$). The absorption feature of Ca II NIR triplet slowly starts developing. As the SN evolves, the above lines become stronger, and the lines due to the iron group elements start appearing in the spectra. In the pre-maximum phase, the profile of Si II ($\lambda 6355$) line is broad and asymmetric with respect to line minimum. This is due to the presence of a high-velocity component in the spectra. The high-velocity feature is usually seen in the Ca II NIR triplet in a significant fraction of type Ia supernova observed during pre-maximum phase

⁶ <https://wiserep.weizmann.ac.il/>

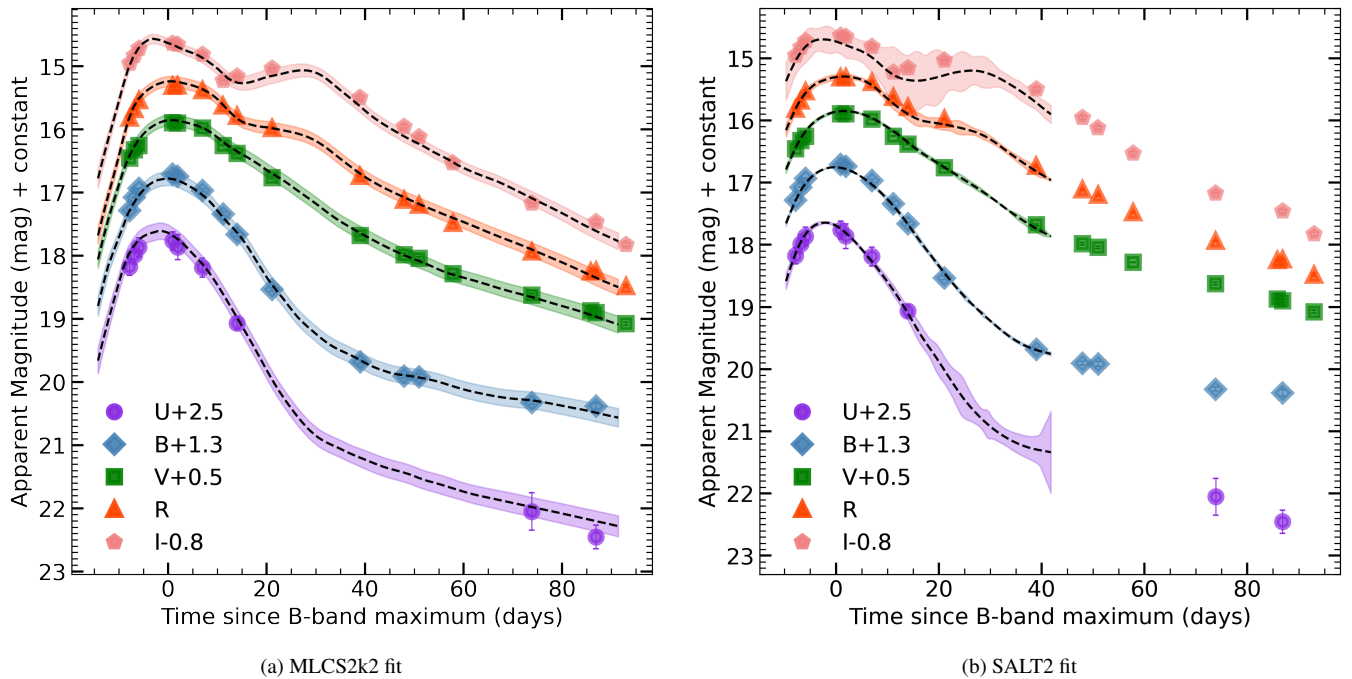


Figure 5. Best fit template light curves to the observed $UBVR$ light curves of SN 2017hpa.

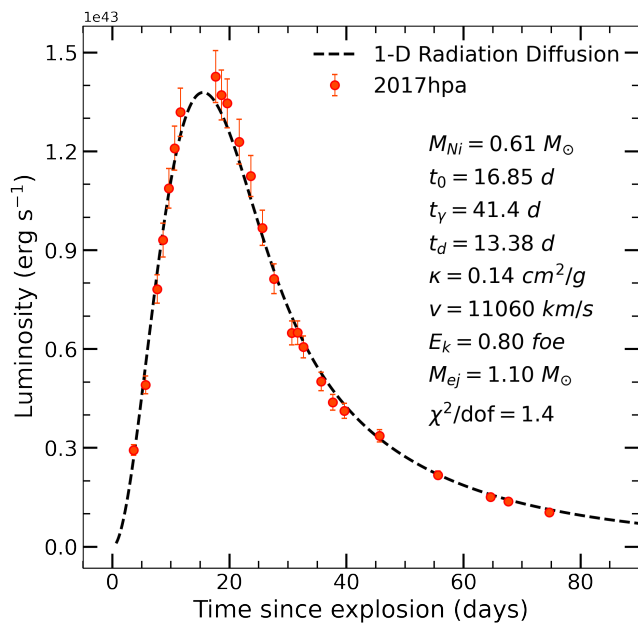


Figure 6. The bolometric light curve of SN 2017hpa plotted along with the 1-D Radiation Diffusion model fit.

(Maguire et al. 2014; Mulligan & Wheeler 2017). In the emission wing of the Si II $\lambda 6355$ line, a prominent absorption feature is seen at ~ 6300 Å which is due to blueshifted C II ($\lambda 6580$) absorption feature. This can be explained by the presence of unburned C that is attributed to subsonic burning (deflagration wave) in a significant fraction of the white dwarf (Röpke et al. 2007).

The spectrum at -13.8 d shows weak blended lines of Fe II ($\lambda 4924$, 5018), Fe III ($\lambda 4421$, 5075, 5158), Co II ($\lambda 4161$) Mg II ($\lambda 4481$, 7890), S II ($\lambda 4716$, 5032, 5321, 5429, 5454, 5510), Si II

($\lambda 4128$, 5972, 6355), Si III ($\lambda 4568$), which become prominent around the maximum. Also, Si II ($\lambda 5972$) starts appearing at -6 d. Strong Si II ($\lambda 6355$) line and weak Si II ($\lambda 5972$) indicate that the photosphere is hot.

The pre-maximum spectrum of SN 2017hpa at -8.9 d is compared with those of SN 2003du (Blondin et al. 2012), SN 2005cf (Garavini et al. 2007), SN 2009dc (Taubenberger et al. 2011), SN 2011fe (Zhang et al. 2016). Among these events, SN 2003du, SN 2005cf and SN 2011fe are normal type Ia SNe, whereas SN 2009dc belongs to the super-Chandrasekhar mass category. All the compared spectra (see Fig. 7 bottom panel) exhibit C II ($\lambda 6580$) absorption feature during this phase. However, the C II ($\lambda 6580$) feature is more prominent in SN 2017hpa than normal SNe Ia, similar to SN 2009dc. By fitting a Gaussian to the absorption feature of C II $\lambda 6580$, we estimate that the pEW of C II evolves from 13.56 ± 1.49 Å at -13.8 d to 4.49 ± 0.43 Å at -5.9 d. The Si II $\lambda 5972$ line is weaker than other objects at this phase. The IME signatures are weak in SN 2017hpa while these are prominent in other objects (see bottom panel of Fig. 7). The relatively weak IME features suggest ongoing burning (Benetti et al. 2004; Taubenberger et al. 2011). The line formation not only depends on the composition but also on the ionisation state of the ejecta. The weakness of the singly ionised IME features can also be explained by higher temperature and in turn, higher ionisation.

The flat-bottom, broad profile of Si II $\lambda 6355$ (at -13.8 d, -8.9 d and -7.8 d) and the asymmetric profile (at -6.8 d and -5.9 d) is most likely due to a high velocity component detached from the photosphere. A high velocity component in Si II has been observed in other well studied type Ia SNe like SN 1990N (Mazzali 2001), SN 2003du (Anupama et al. 2005; Tanaka et al. 2011), SN 2005cf (Wang et al. 2009a), SN 2009ig (Foley et al. 2012; Marion et al. 2013), SN 2012fr (Childress et al. 2013), SN 2019ein (Kawabata et al. 2020; Pellegrino et al. 2020). By fitting a Gaussian to the absorption profile of Si II ($\lambda 6355$) and Si II ($\lambda 5972$) at -5.9 d we estimate the pEW of Si II ($\lambda 5972$) to be 13.75 ± 1.70 Å and that of Si II ($\lambda 6355$) to be 67.22 ± 4.88 Å, implying a ratio $R(\text{Si II})$ of 0.20 ± 0.03 .

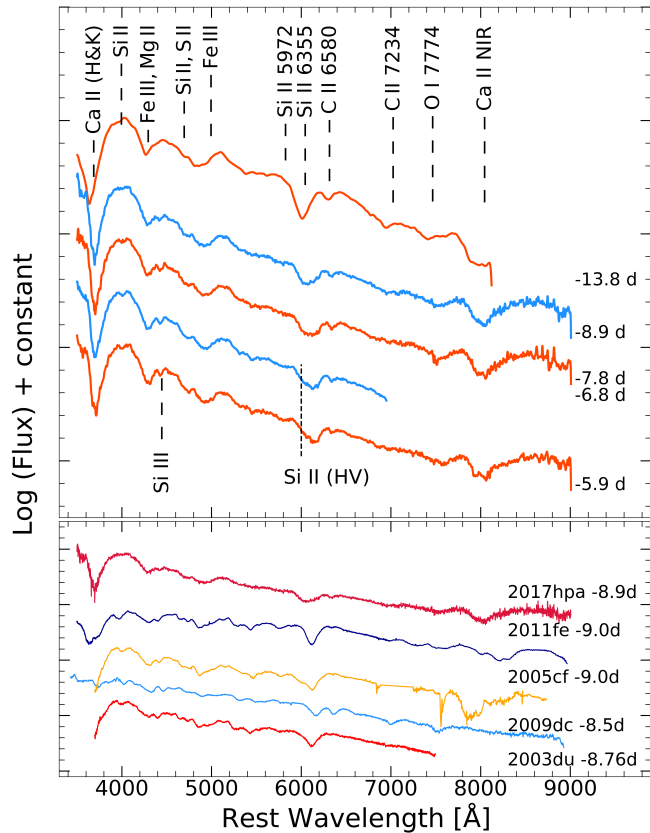


Figure 7. Top panel: Evolution of the pre-maximum spectrum of SN 2017hpa. The -13.8 d spectrum downloaded from WISEReP is also plotted. Bottom panel: The -8.9 d spectrum of SN 2017hpa has been compared with SN 2011fe, SN 2009dc, SN 2005cf and SN 2003du around similar phase. The spectra have been smoothed while plotting to enhance visibility of the features.

At $+0.9$ d the pEW of Si II ($\lambda 5972$) is 9.22 ± 1.02 Å that of Si II ($\lambda 6355$) is 75.16 ± 1.96 Å and $R(\text{Si II})$ is 0.13 ± 0.02 . From the value of $R(\text{Si II})$, SN 2017hpa can be placed among the Core-Normal (CN) class described by Branch et al. (2006).

4.2 Maximum and early post-maximum phase

The spectral evolution during the maximum and early post-maximum phase is presented in Fig. 8. The C II ($\lambda 6580$) line seen in the pre-maximum phase is not seen in the spectrum taken close to maximum. Around this phase, the IME features have become prominent. The 'W' feature due to S II ($\lambda 5468, 5654$) line is prominent in the maximum spectrum, and it becomes weak in the spectrum taken at $+11$ d. The high-velocity feature in the Si II ($\lambda 6355$) line seen during the pre-maximum phase disappears close to maximum, and the photospheric component is dominant. Because of the high-velocity feature in the Ca II NIR triplet, the absorption feature shows two minima till $+2$ d and it is not seen in the next spectrum taken at $+11$ d. The Si III ($\lambda 4568$) line was seen in the spectrum till $+2$ d but was not present in the later spectra. The spectrum of SN 2017hpa close to the maximum is compared with the spectra of some other well studied SNe (see bottom panel of Fig. 8) and is found to be similar.

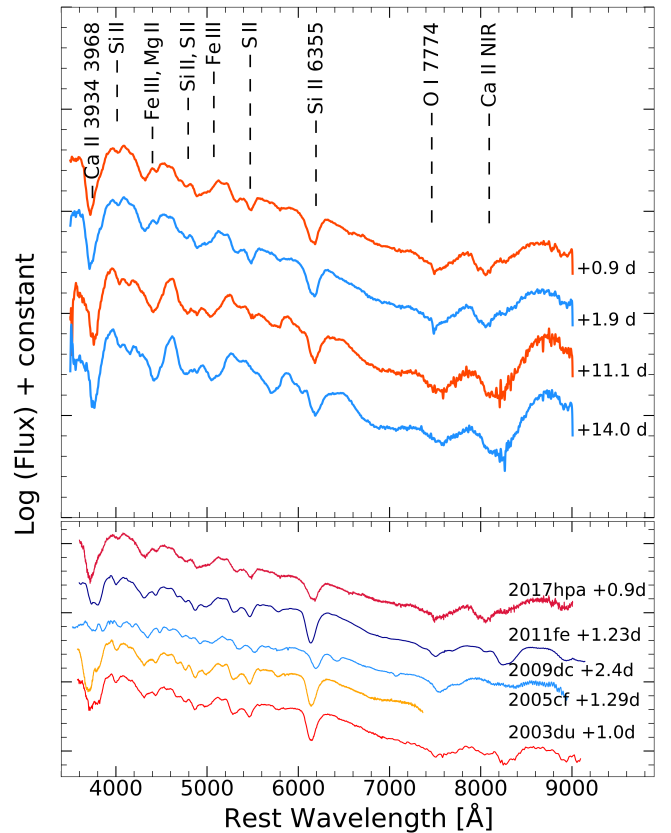


Figure 8. Top panel: Spectral evolution of SN 2017hpa around maximum. Bottom panel: The $+0.9$ d spectrum of SN 2017hpa has been compared with SN 2011fe, SN 2009dc, SN 2005cf and SN 2003du around similar phase. The spectra have been smoothed while plotting to enhance visibility of the features.

4.3 Post-maximum to early nebular phases

The spectral evolution of SN 2017hpa during post-maximum to early nebular phases is presented in Fig. 9 and Fig. 10. It is evident from Fig. 9 that the Si II line is weakening, and Fe II ($\lambda 6238, 6248$) lines are getting stronger. The pEW of Si II ($\lambda 6355$) evolves from 75.16 ± 1.96 at $+0.9$ d to 57.04 ± 1.38 at $+14.0$ d. This weakening of the Si II feature indicates that the ejecta is diluting and the SN enters into the Fe II dominated phase. Further, the Ca II H & K feature begins to weaken around $+23$ d. In contrast, the Ca II NIR triplet remains a broad, flat bottom absorption profile with a pronounced emission component until $+57$ d.

During the late post maximum phase to the early nebular phase, the ejecta begins to get transparent, and the inner regions of the explosion can be probed. The Fe II absorption feature at $\lambda 4555$ remains prominent, and the Fe II lines at $\lambda 4924$ and $\lambda 5018$ are clearly seen till $+58.0$ d. The Fe II line at $\lambda 5169$ shows a deep absorption feature at 5100 Å, and to the redward wing, the Fe II $\lambda 5536$ line can be seen as a prominent notch. Around 6000 Å there are blended lines of Fe II $\lambda 6238, \lambda 6248$ and $\lambda 6451, \lambda 6456$. Fe II lines at $\lambda 7308$ and $\lambda 7462$ are weak. In the bottom panel of Fig. 9 the $+39.0$ day spectra of SN 2017hpa has been compared with SN 2014J (Srivastav et al. 2016), SN 2009dc, SN 2005cf, SN 2003du and SN 2002bo around similar phases.

The spectrum at $+74.0$ d shows strong forbidden emission lines due to Fe and Co. This shows that the SN has entered into the nebular phase (Dessart et al. 2014b). Early nebular phase spectra show

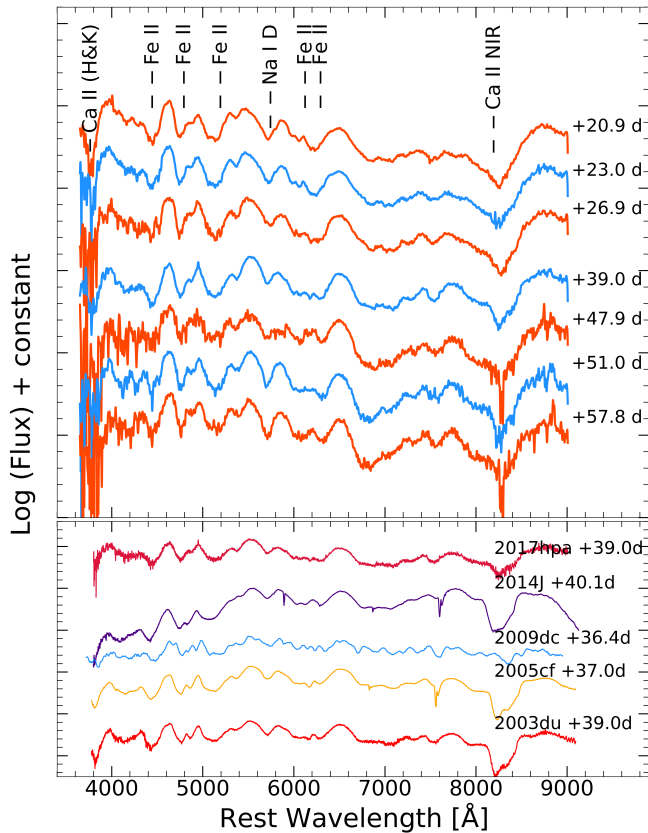


Figure 9. Top panel: Post maximum spectral evolution of SN 2017hpa. Bottom panel: The +39.0 d spectrum of SN 2017hpa has been plotted with SN 2014J, SN 2009dc, SN 2005cf, SN 2003du for comparison. The spectra have been smoothed while plotting to enhance visibility of the features.

features of [Fe III], [Fe II], [Ni II], [Co III]. The strongest feature seen in the nebular phase spectra is the emission at $\lambda 4700$, which is due to a blend of several [Fe III] lines with some contribution from [Fe II]. The emission line seen around 5100 \AA in our early nebular phase spectra is due to contributions from [Fe II] and [Fe III] lines. In the very early nebular phase spectra, the [Co III] emission line at around 5900 \AA is quite strong, but as the supernova ages, the [Co III] lines become weaker due to decay of ^{56}Co to ^{56}Fe . In the bottom panel of Fig. 10 the +86.8 d spectrum of SN 2017hpa has been compared with SN 2014J, SN 2005cf and SN 2003du. The [Fe II] emission feature around 4700 \AA at +86.8 d is stronger in the spectrum of SN 2017hpa than the comparison SNe.

4.4 Velocity Evolution

The velocity of the spectral lines has been measured by fitting a single Gaussian function to the absorption trough of the corresponding lines. The velocities of Ca II (H & K) $\lambda 3951$, Si II $\lambda 6355$, C II $\lambda 6580$ lines estimated based on the absorption minimum are plotted in Fig. 11 (left panel). The most prominent line in the spectra, Si II $\lambda 6355$ traces the evolution of the expansion velocity of the ejecta for over 4–5 weeks since the explosion. The Si II line has a velocity of $16,150 \pm 160 \text{ km s}^{-1}$ around -13 d , which is quite normal for type Ia SNe around this phase. The Si II line velocity drops rapidly to $9400 \pm 140 \text{ km s}^{-1}$ close to maximum. The subsequent decline is slow, reaching a velocity of $\sim 8000 \text{ km s}^{-1}$ at +15 d.

The C II ($\lambda 6580$) absorption feature evolves from $12,720 \pm 220 \text{ km}$

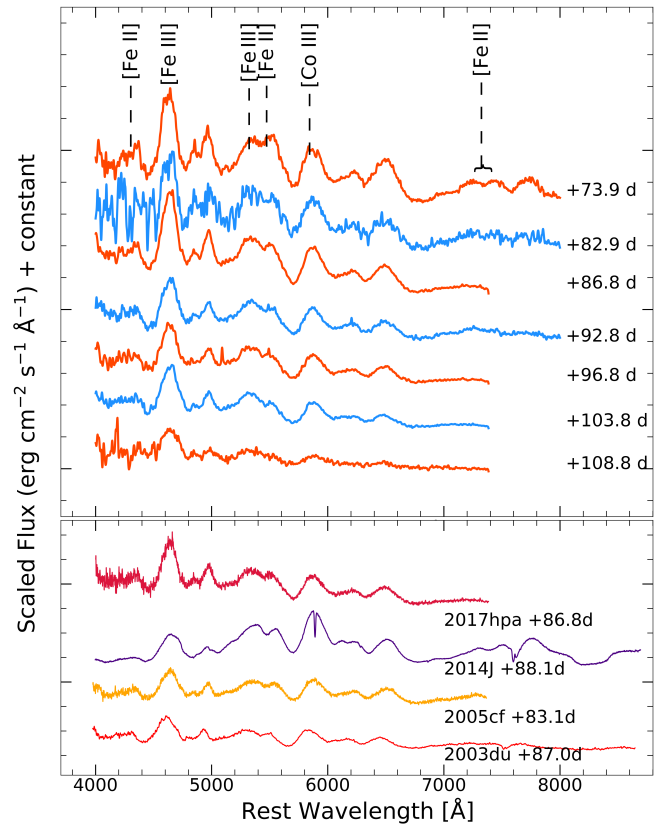


Figure 10. Top panel: Spectral evolution of SN 2017hpa in the early nebular phase. Bottom panel: The +86.8 d spectrum of SN 2017hpa has been compared with SN 2014J, SN 2005cf and SN 2003du around similar phases for comparison. The spectra have been smoothed while plotting to enhance visibility of the features.

s^{-1} to $10,670 \pm 180 \text{ km s}^{-1}$ (Fig 11). The measured C II $\lambda 6580$ line velocity is significantly lower than Si II $\lambda 6355$, with the $v_{\text{CII}}/v_{\text{SiII}}$ ratio varying from ~ 0.78 on day -13.8 to ~ 0.91 on day -5.9 . This variation in the velocity ratio is dissimilar with the results of Parrent et al. (2011), who have shown the ratio to be constant over time, in a sample of 19 SNe Ia. Their sample also indicates the ratio to be ~ 1 within 10%. The discrepancy between the photospheric velocity (as measured by Si II velocity) and the carbon velocity is explained by Parrent et al. (2011) as being due to a clumpy carbon layer that is offset by an angle θ from the line of sight. The angle can be estimated if $v_{\text{CII}} < v_{\text{SiII}}$. The observed velocity ratios indicate θ to be $\sim 40^\circ$ on day -13.8 and $\sim 25^\circ$ on day -5.9 . It is suggested that the change in the ratio (and angle from the line of sight) is indicative of an initial asymmetry that became more symmetric as the SN ejecta evolved. Another possible explanation for the lower velocity ratio is mixing within the ejecta. The Ca II (H & K) $\lambda 3951$ absorption feature is seen to be around $\sim 22,000 \text{ km s}^{-1}$ at -13.8 d and always remains higher than Si II $\lambda 6355$.

Benetti et al. (2005) made a hierarchical cluster analysis of SN Ia based on both photometric ($\Delta m_{15}(B)$, M_B) and spectroscopic (\dot{v} , $v_{10}(\text{Si II})$, $R(\text{Si II})_{\text{max}}$) parameters of SNe. Here, \dot{v} is the average daily decline rate of expansion velocity of Si II $\lambda 6355$ line, derived from the least square fit to the measurements taken between maximum and either the time the Si II feature disappears or the last available spectrum, whichever is earlier. The velocity of Si II, 10 days past maximum is denoted as v_{10} .

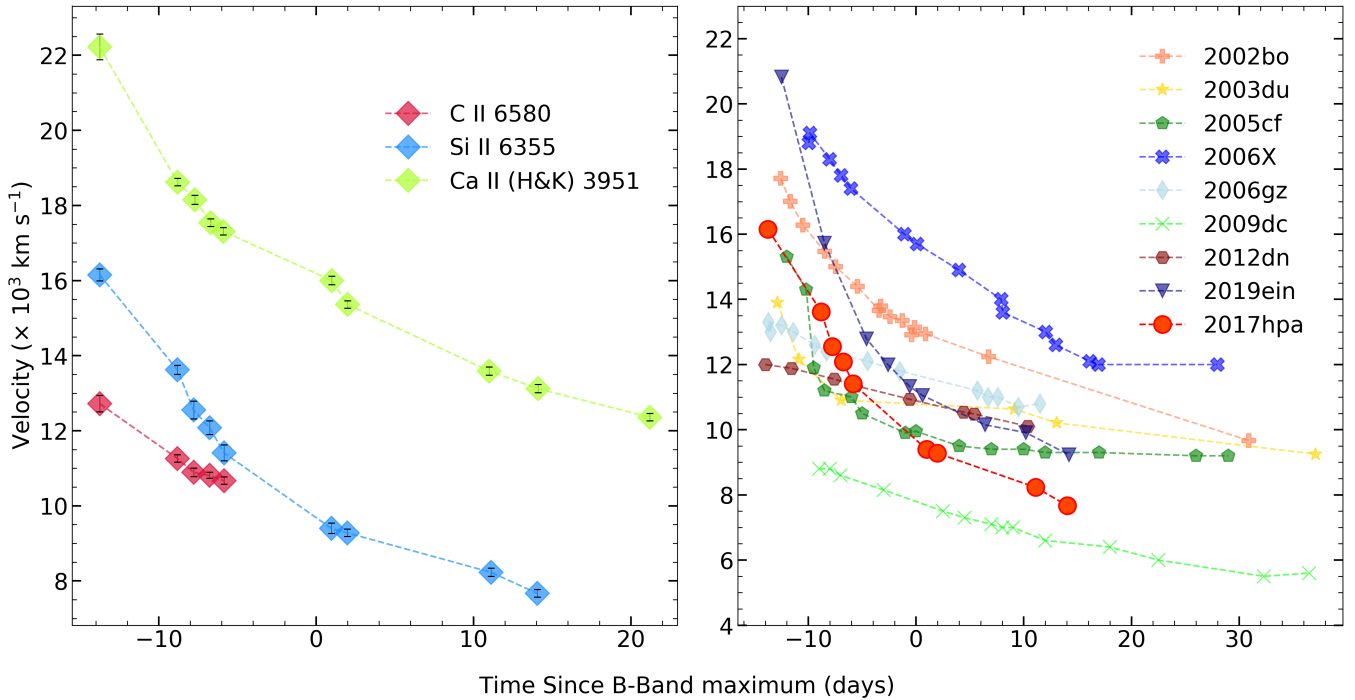


Figure 11. Velocity evolution of C II λ 6580, Si II λ 6355 and Ca II λ 3951 for SN 2017hpa (left panel). Comparison of the velocity evolution of Si II λ 6355 for SN 2017hpa with other SNe Ia (right panel).

From the velocity evolution of SN 2017hpa, values of \dot{v} , v_{10} and velocity at maximum are estimated as $127.9 \pm 6.1 \text{ km s}^{-1} \text{d}^{-1}$, $\sim 8320 \text{ km s}^{-1}$ and $\sim 9640 \text{ km s}^{-1}$, respectively. With the measured value of \dot{v} , SN 2017hpa can be placed under the HVG group of Benetti et al. (2005) scheme. It is worth mentioning that the average value of v_{10} for the HVG group is $12200 \pm 1100 \text{ km s}^{-1}$ which is significantly higher than v_{10} estimated for SN 2017hpa ($\sim 8320 \text{ km s}^{-1}$). Based on the photometric and spectroscopic properties, SN 2017hpa can be placed under normal Ia with HVG.

The Si II λ 6355 line velocity evolution is plotted along with other high-velocity gradient and normal SNe (see Fig. 11, right panel). For SN 2003du, and SN 2005cf, it is seen that the post maximum velocity evolution is flat. From the velocity evolution, sometimes the channel of explosion can be inferred.

Foley et al. (2011) used a linear fit to the data between $-6 \leq t \leq 10 \text{ d}$. The slope gives the velocity gradient, and the offset (v^0) is the velocity at B-band maximum. Using this relation, the velocity gradient has been found to be $306.9 \pm 25.1 \text{ km s}^{-1} \text{d}^{-1}$ and $v^0 \sim 9870 \text{ km s}^{-1}$. Using the expansion velocity of Si II λ 6355 at maximum Wang et al. (2009b) classified SNe Ia into two broad groups, High Velocity (HV, $v \geq 11,800 \text{ km s}^{-1}$ and Normal Velocity ($10,600 \pm 400 \text{ km s}^{-1}$). According to this, SN 2017hpa clearly falls in the Normal velocity group.

4.5 Spectral Fitting in the pre-maximum phase

The spectral features in the pre-maximum spectra at phases -13.8 day and -8.9 day are identified using synthetic spectra generated using the *syn++*⁷ code (Parent et al. 2010; Thomas et al. 2011a). The synthetic spectra are also used to obtain an estimate of the velocity

distribution. The code is based upon simple assumptions of spherical symmetry, homologous expansion, a sharp photosphere that emits a continuous blackbody spectrum, line formation by resonant scattering assuming Sobolev approximation. The synthetic spectrum consists of blended P-Cygni profiles superimposed on a continuum. The code has been extensively used for line identifications, estimating the velocity of the pseudophotosphere and constraining the velocity interval over which lines due to various ions are formed. For each ion introduced into the fitting, the optical depth at the photospheric velocity is a fitting parameter. The optical depth of other lines are calculated assuming Boltzmann excitation temperature (T_{exc}). The optical depths of lines are taken to be exponentially decreasing function of velocity with the e-folding velocity (aux). At each epoch, the important fitting parameters are the velocity at the photosphere (v_{phot}), the optical depth of the ion reference line (τ), the minimum and maximum velocity (v_{min} & v_{max}) imposed on the ions. When the minimum velocity exceeds the photosphere's velocity, then the ion is said to be detached. The blackbody fit temperature (T_{BB}) represents the overall shape of the spectrum.

The spectrum at -13.8 day is fit with photospheric velocity of $\sim 15,000 \text{ km s}^{-1}$ and blackbody temperature of $10,000 \text{ K}$ to match the slope of the observed spectrum. The temperature is consistent with that obtained by fitting a blackbody to the photometric spectral energy distribution (SED). The spectrum is fit with ions of IME's like C II, Mg II, Si II (PV & HV), Ca II (PV & HV) and IGE's like Fe II and Fe III. An excitation temperature of $10,000 \text{ K}$ and a maximum velocity of $30,000 \text{ km s}^{-1}$ have been used for all the ions. To fit the Si II λ 6355 line profile in the observed spectrum, a high velocity component at $22,000 \text{ km s}^{-1}$ has been introduced. From the fit to the spectrum, it is evident that both the C II λ 6580 and Si II λ 6355 features can be reproduced with a photospheric velocity of $15,000 \text{ km s}^{-1}$. This indicates that the line forming region of Si II and C II are moving at the same velocity. The Ca II (H & K) profile is also

⁷ <https://c3.lbl.gov/es/>

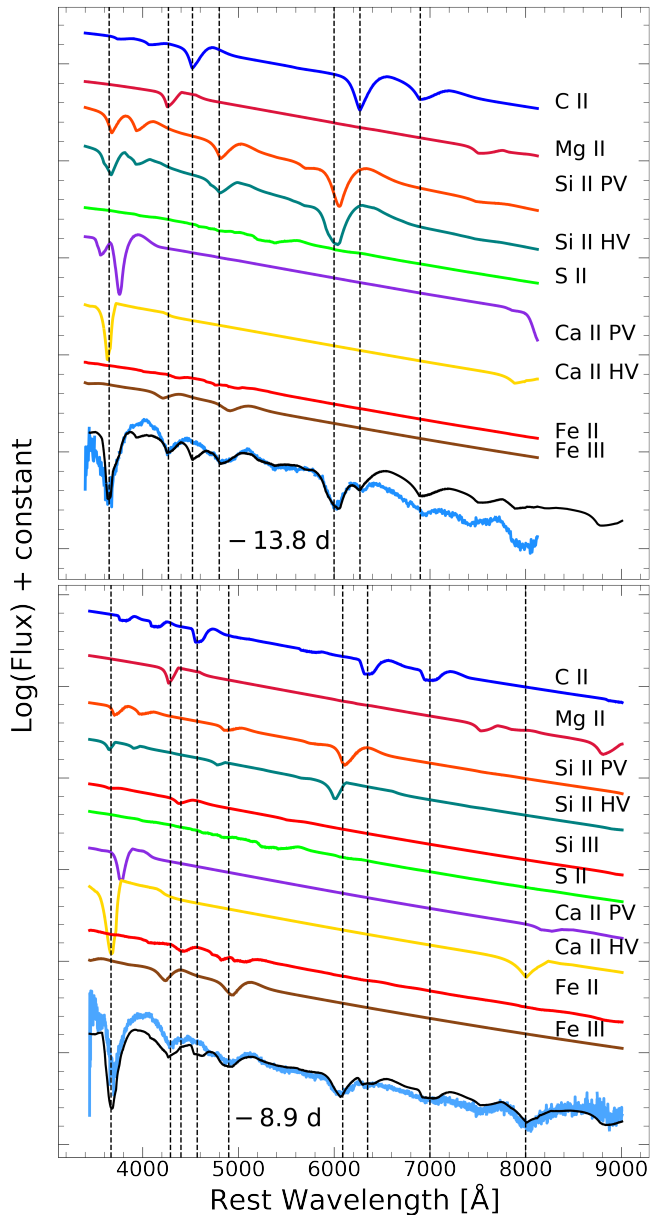


Figure 12. Dereddened and redshift corrected spectra of SN 2017hpa at -13.8 d and -8.9 d, plotted along with the synthetic spectra (black solid line) generated using *syn++*. The contributions from each element are shown.

fitted with two components, one at $17,000 \text{ km s}^{-1}$ and another, high-velocity component, with a velocity of $25,000 \text{ km s}^{-1}$.

The spectrum at -8.9 d is fit with a photospheric velocity of $13,800 \text{ km s}^{-1}$ and a blackbody temperature of $11,000 \text{ K}$. In this phase also, the observed Si II $\lambda 6355$ feature can be reproduced by a combination of the photospheric component and a high velocity component at $18,000 \text{ km s}^{-1}$. The C II feature is fit with a velocity of $13,800 \text{ km s}^{-1}$, similar to the photospheric component of Si II. Si III ($\lambda 4553, 4568, 4575$) features are well reproduced with the photospheric velocity of $13,800 \text{ km s}^{-1}$. The spectral fits are shown in Fig. 12.

Most of the prominent features observed in the spectra of 2017hpa in the pre-maximum phase are reproduced in the *syn++* synthetic spectra. We note that certain components will require careful fitting in an iterative way. The details of the fit are provided in Table A5.

To study the explosion mechanism and to put a constraint on the mass of unburned C present in the ejecta, we applied the one-dimensional spectrum synthesis code *TARDIS* (Kerzendorf & Sim 2014) to our spectrum at -8.9 d. The fit parameters of *TARDIS* are listed in Table A6. *TARDIS* takes as input the luminosity of the SN, the time since the explosion, a density, velocity and abundance profile. *TARDIS* assumes a single, sharp photosphere is emitting a quasi-blackbody continuum between the optically thick and thin regions of the ejecta. For a uniform abundance, the region above the photosphere is divided into multiple, spherically symmetric cells. By specifying the mass fraction of the elements as inputs in these cells, *TARDIS* generates a synthetic spectrum by calculating the ionisation and excitation states. In this work, we model the spectrum by using a uniform abundance of elements, and a W7-like (Nomoto et al. 1984; Branch et al. 1985) density profile. The observed spectrum does not have prominent lines due to IGE’s; hence we consider only C, O, Mg, Si and Ca for fitting the observed spectrum. By using a uniform composition in all the cells, a satisfactory fit to the observed spectrum was not possible in the entire wavelength range. Since we observe strong C feature in the pre-maximum spectra around $\lambda 6580$, we tried to put a constraint on the mass of unburned C. An attempt is made to fit the region around Si II and C II by varying the mass fraction of C from 0.01 to 0.04 and keeping the mass fraction of other elements the same (see Fig. 13). It is found that for the mass fraction of C more than 0.03, the C II line blends with Si II, hence we put an upper limit to the C mass fraction as 0.03. By integrating the contribution from all cells, we find $\sim 0.019 M_{\odot}$ of C in the outer regions of the ejecta, which is consistent with the mass estimate by Tanaka et al. (2011) for SN 2003du. The estimated carbon mass is significantly lower than the mass expected in a deflagration model ($0.049 M_{\odot}$). This could be due to mixing in the ejecta.

5 SUMMARY

The properties of SN 2017hpa make it an interesting object. From the photometric and spectroscopic properties, it can be classified as a normal type Ia object with $\Delta m_{15}(B) = 0.98 \pm 0.16$ and $M_B^{max} = -19.45 \pm 0.15$ with a distinct secondary maximum in *I* band. With standard light curve fitting methods like MLCS2k2 and SALT2, the distance modulus is estimated to be 34.08 ± 0.09 with a host reddening of $E(B-V) = 0.08$ and an R_V of 1.9. The $(B-V)$ colour evolution is bluer than the comparison SNe, and from the $(uvw1 - uvv)$ colour evolution, SN 2017hpa can be placed under NUV-blue group. By fitting the bolometric light curve with the radiation diffusion model, we derive nickel mass (M_{Ni}) of $0.61 M_{\odot}$ and ejecta mass of $1.10 M_{\odot}$.

The pre-maximum spectral sequence of SN 2017hpa shows a relatively featureless continuum. The spectral evolution shows strong C II $\lambda 6580$ line, which can be seen until 5.9 days before maximum. The observed velocity of C II is lower than Si II $\lambda 6355$. However the *syn++* fit to the observed spectra shows that both the C II and Si II line forming regions are moving with the photospheric velocity. The Si II $\lambda 6355$ shows rapid evolution in velocity and the velocity gradient measured is $127.9 \pm 6.1 \text{ km s}^{-1} \text{ d}^{-1}$ which places SN 2017hpa among the HVG objects according to the Benetti classification scheme. The velocity measured at the maximum is $\sim 9643 \text{ km s}^{-1}$ which is clearly within the range for normal velocity SNe Ia. Typically, C II is associated with the low-velocity gradient group (Blondin et al. 2012). The $(B-V)$ colour at maximum is redder for the HVG subtype (Stritzinger et al. 2018). The observed properties of SN 2017hpa are strikingly opposite to this. *TARDIS* model fit to our spectrum requires unburned C mass to be $\sim 0.019 M_{\odot}$, lower than that expected by de-

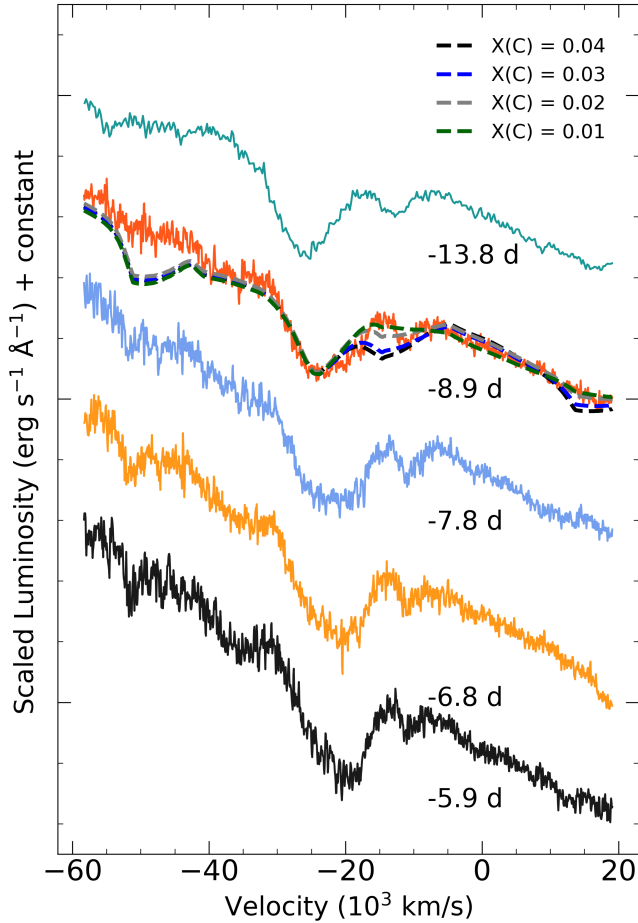


Figure 13. Velocity evolution of C II $\lambda 6580$. The velocity is defined with respect to rest wavelength of C II $\lambda 6580$. The dotted solid lines indicate *TARDIS* fit to the observed spectra with different mass fraction for Carbon.

flagration alone. Detailed three-dimensional modelling may confirm the exact nature of SN 2017hpa.

ACKNOWLEDGEMENTS

We thank the referee for going through the manuscript carefully and providing constructive suggestions which helped in improving the content of the paper. We thank the staff of IAO, Hanle and CREST, Hosakote that made the observations possible. The facilities at IAO and CREST are operated by the Indian Institute of Astrophysics, Bangalore. We also thank the observers who shared their valuable time in Target of Opportunity (ToO) observations during the initial follow up. This work has made use of the NASA Astrophysics Data System⁸ (ADS), the NASA/IPAC extragalactic database⁹ (NED) and NASA/IPAC Infrared Science Archive (IRSA)¹⁰ which is operated by the Jet Propulsion Laboratory, California Institute of Technology. We acknowledge, Weizmann Interactive Supernova Data REPOSITORY¹¹ (WISeREP, Yaron & Gal-Yam (2012)). The research has made use of the data obtained from the High Energy Astrophysics Science

⁸ <https://ui.adsabs.harvard.edu/>

⁹ <https://ned.ipac.caltech.edu/>

¹⁰ <https://irsa.ipac.caltech.edu/applications/DUST/>

¹¹ <https://wiserep.weizmann.ac.il/>

Archive Research Center (HEASARC)¹², a facility of the Astrophysics Science Division at NASA/GSFC and of the Smithsonian Astrophysical Observatory's High Energy Astrophysics Division. This research made use of *Tardis*, a community-developed software package for spectral synthesis in supernovae (Kerzendorf & Sim 2014; Kerzendorf et al. 2019). The development of *Tardis* received support from the Google Summer of Code initiative and from ESA's Summer of Code in Space program. *Tardis* makes extensive use of *Astropy* and *PyNE*. The reduction of photometric and spectroscopic data has been greatly facilitated by *REDPIPE*¹³. The analysis has made use of the following software and packages - (i) *Image Reduction and Analysis Facility (IRAF)*, Tody (1993). (ii) *PyRAF*, Science Software Branch at STScI (2012). (iii) *NumPy*, Van Der Walt et al. (2011), (iv) *Matplotlib*, Hunter (2007), (v) *SciPy*, Virtanen et al. (2020), (vi) *pandas*, pandas development team (2020), (vii) *astropy*, Astropy Collaboration et al. (2013), (viii) *emcee*, Foreman-Mackey et al. (2013a), (ix) *syn++*, Thomas et al. (2011a), (x) *TARDIS*, Kerzendorf & Sim (2014).

DATA AVAILABILITY

The UV and Optical magnitudes are tabulated in Table A2 and A3, respectively. The log of spectroscopic data is provided in Table A4. The *Swift*–*UVOT* data are available at https://www.swift.ac.uk/swift_portal/. The spectroscopic data used in this work will be made available on request.

REFERENCES

- Anupama G. C., Sahu D. K., Jose J., 2005, *A&A*, **429**, 667
 Arnett W. D., 1982, *ApJ*, **253**, 785
 Astropy Collaboration et al., 2013, *A&A*, **558**, A33
 Benetti S., et al., 2004, *MNRAS*, **348**, 261
 Benetti S., et al., 2005, *ApJ*, **623**, 1011
 Bessell M. S., Castelli F., Plez B., 1998, *A&A*, **333**, 231
 Betoule M., et al., 2014, *A&A*, **568**, A22
 Blondin S., et al., 2012, *AJ*, **143**, 126
 Branch D., Doggett J. B., Nomoto K., Thielemann F. K., 1985, *ApJ*, **294**, 619
 Branch D., et al., 2006, *PASP*, **118**, 560
 Brown P. J., et al., 2009, *AJ*, **137**, 4517
 Burns C. R., et al., 2020, *ApJ*, **895**, 118
 Chatzopoulos E., Wheeler J. C., Vinko J., 2012, *ApJ*, **746**, 121
 Childress M. J., et al., 2013, *ApJ*, **770**, 29
 Clocchiatti A., Wheeler J. C., 1997, *ApJ*, **491**, 375
 Contardo G., Leibundgut B., Vacca W. D., 2000, *A&A*, **359**, 876
 Dessart L., Blondin S., Hillier D. J., Khokhlov A., 2014a, *MNRAS*, **441**, 532
 Dessart L., Hillier D. J., Blondin S., Khokhlov A., 2014b, *MNRAS*, **441**, 3249
 Fitzpatrick E. L., 1999, *PASP*, **111**, 63
 Floers A., Taubenberger S., Vogl C., Tomasella L., Benetti S., Cappellaro E., 2017, *The Astronomer's Telegram*, **10896**, 1
 Folatelli G., et al., 2012, *ApJ*, **745**, 74
 Foley R. J., Sanders N. E., Kirshner R. P., 2011, *ApJ*, **742**, 89
 Foley R. J., et al., 2012, *ApJ*, **744**, 38
 Foreman-Mackey D., et al., 2013a, *emcee*: The MCMC Hammer (ascl:1303.002)
 Foreman-Mackey D., Hogg D. W., Lang D., Goodman J., 2013b, *PASP*, **125**, 306
 Gagliano R., Post R., Weinberg E., Newton J., Puckett T., 2017, *Transient Name Server Discovery Report*, **2017-1164**, 1

¹² <https://heasarc.gsfc.nasa.gov/>

¹³ <https://github.com/sPaMFoUR/RedPipe>

- Garavini G., et al., 2007, *A&A*, 471, 527
- Goldstein D. A., Kasen D., 2018, *ApJ*, 852, L33
- Han X., et al., 2020, *ApJ*, 892, 142
- Hicken M., et al., 2009, *ApJ*, 700, 331
- Hoeflich P., Khokhlov A. M., Wheeler J. C., 1995, *ApJ*, 444, 831
- Horne K., 1986, *PASP*, 98, 609
- Hosseinzadeh G., et al., 2017, *ApJ*, 845, L11
- Hoyle F., Fowler W. A., 1960, *ApJ*, 132, 565
- Hunter J. D., 2007, *Computing in Science & Engineering*, 9, 90
- Iben I. J., Tutukov A. V., 1984, *ApJS*, 54, 335
- Jha S., Riess A. G., Kirshner R. P., 2007, *ApJ*, 659, 122
- Kasen D., 2006, *ApJ*, 649, 939
- Kasen D., Röpke F. K., Woosley S. E., 2009, *Nature*, 460, 869
- Kawabata M., et al., 2020, *ApJ*, 893, 143
- Kerzendorf W. E., Sim S. A., 2014, *MNRAS*, 440, 387
- Kerzendorf W., et al., 2019, tardis-sn/tardis: TARDIS v3.0 alpha2, doi:10.5281/zenodo.2590539
- Khokhlov A. M., 1991, *A&A*, 245, L25
- Könyves-Tóth R., et al., 2020, *ApJ*, 892, 121
- Kromer M., Sim S. A., Fink M., Röpke F. K., Seitenzahl I. R., Hillebrandt W., 2010, *ApJ*, 719, 1067
- Landolt A. U., 1992, *AJ*, 104, 340
- Lentz E. J., Baron E., Branch D., Hauschildt P. H., Nugent P. E., 2000, *ApJ*, 530, 966
- Li W., et al., 2019, *ApJ*, 870, 12
- Lira P., et al., 1998, *AJ*, 115, 234
- Maeda K., et al., 2010, *Nature*, 466, 82
- Maguire K., et al., 2014, *MNRAS*, 444, 3258
- Marion G. H., et al., 2013, *ApJ*, 777, 40
- Mazzali P. A., 2001, *MNRAS*, 321, 341
- Milne P. A., Brown P. J., Roming P. W. A., Bufano F., Gehrels N., 2013, *ApJ*, 779, 23
- Mulligan B. W., Wheeler J. C., 2017, *MNRAS*, 467, 778
- Nomoto K., 1982a, *ApJ*, 253, 798
- Nomoto K., 1982b, *ApJ*, 257, 780
- Nomoto K., Thielemann F. K., Yokoi K., 1984, *ApJ*, 286, 644
- Nugent P., Phillips M., Baron E., Branch D., Hauschildt P., 1995, *ApJ*, 455, L147
- Pakmor R., Kromer M., Taubenberger S., Springel V., 2013, *ApJ*, 770, L8
- Parrent J., Branch D., Jeffery D., 2010, SYNOW: A Highly Parameterized Spectrum Synthesis Code for Direct Analysis of SN Spectra (ascl:1010.055)
- Parrent J. T., et al., 2011, *ApJ*, 732, 30
- Pellegrino C., et al., 2020, *ApJ*, 897, 159
- Perlmutter S., et al., 1999, *ApJ*, 517, 565
- Phillips M. M., 1993, *ApJ*, 413, L105
- Phillips M. M., Lira P., Suntzeff N. B., Schommer R. A., Hamuy M., Maza J., 1999, *AJ*, 118, 1766
- Poole T. S., et al., 2008, *MNRAS*, 383, 627
- Poznanski D., Prochaska J. X., Bloom J. S., 2012, *MNRAS*, 426, 1465
- Raskin C., Timmes F. X., Scannapieco E., Diehl S., Fryer C., 2009, *MNRAS*, 399, L156
- Riess A. G., Press W. H., Kirshner R. P., 1995, *ApJ*, 438, L17
- Riess A. G., Press W. H., Kirshner R. P., 1996, *ApJ*, 473, 88
- Riess A. G., et al., 1998a, *AJ*, 116, 1009
- Riess A. G., Nugent P., Filippenko A. V., Kirshner R. P., Perlmutter S., 1998b, *ApJ*, 504, 935
- Röpke F. K., Hillebrandt W., Schmidt W., Niemeyer J. C., Blinnikov S. I., Mazzali P. A., 2007, *ApJ*, 668, 1132
- Schlafly E. F., Finkbeiner D. P., 2011, *ApJ*, 737, 103
- Science Software Branch at STScI 2012, PyRAF: Python alternative for IRAF (ascl:1207.011)
- Silverman J. M., Filippenko A. V., 2012, *MNRAS*, 425, 1917
- Sim S. A., Fink M., Kromer M., Röpke F. K., Ruiter A. J., Hillebrandt W., 2012, *MNRAS*, 420, 3003
- Singh A., Srivastav S., Kumar B., Anupama G. C., Sahu D. K., 2018, *MNRAS*, 480, 2475
- Skrutskie M. F., et al., 2006, *AJ*, 131, 1163
- Srivastav S., Ninan J. P., Kumar B., Anupama G. C., Sahu D. K., Ojha D. K., Prabhu T. P., 2016, *MNRAS*, 457, 1000
- Stalin C. S., Hegde M., Sahu D. K., Parihar P. S., Anupama G. C., Bhatt B. C., Prabhu T. P., 2008, Bulletin of the Astronomical Society of India, 36, 111
- Stanishev V., et al., 2007, *A&A*, 469, 645
- Stetson P. B., 1987, *PASP*, 99, 191
- Stritzinger M. D., et al., 2018, *ApJ*, 864, L35
- Tanaka M., Mazzali P. A., Stanishev V., Maurer I., Kerzendorf W. E., Nomoto K., 2011, *MNRAS*, 410, 1725
- Taubenberger S., et al., 2011, *MNRAS*, 412, 2735
- Thomas R. C., Nugent P. E., Meza J. C., 2011a, *PASP*, 123, 237
- Thomas R. C., et al., 2011b, *ApJ*, 743, 27
- Tody D., 1993, in Hanisch R. J., Brissenden R. J. V., Barnes J., eds, Astronomical Society of the Pacific Conference Series Vol. 52, Astronomical Data Analysis Software and Systems II. p. 173
- Turatto M., Benetti S., Cappellaro E., 2003, in Hillebrandt W., Leibundgut B., eds, From Twilight to Highlight: The Physics of Supernovae. p. 200 (arXiv:astro-ph/0211219), doi:10.1007/10828549_26
- Valenti S., et al., 2008, *MNRAS*, 383, 1485
- Van Der Walt S., Colbert S. C., Varoquaux G., 2011, Computing in Science & Engineering, 13, 22
- Vinkó J., et al., 2012, *A&A*, 546, A12
- Virtanen P., et al., 2020, *Nature Methods*, 17, 261
- Wang X., et al., 2009a, *ApJ*, 697, 380
- Wang X., et al., 2009b, *ApJ*, 699, L139
- Webbink R. F., 1984, *ApJ*, 277, 355
- Wee J., Chakraborty N., Wang J., Penprase B. E., 2018, *ApJ*, 863, 90
- Wheeler J. C., Johnson V., Clocchiatti A., 2015, *MNRAS*, 450, 1295
- Yaron O., Gal-Yam A., 2012, *PASP*, 124, 668
- Zhang J.-J., Wang X.-F., Bai J.-M., Zhang T.-M., Wang B., Liu Z.-W., Zhao X.-L., Chen J.-C., 2014, *AJ*, 148, 1
- Zhang K., et al., 2016, *ApJ*, 820, 67
- pandas development team T., 2020, pandas-dev/pandas: Pandas, doi:10.5281/zenodo.3509134, https://doi.org/10.5281/zenodo.3509134

APPENDIX A: TABLES

Table A1. *UBVRI* magnitudes of local standards in the field of SN 2017hpa.

ID	<i>U</i>	<i>B</i>	<i>V</i>	<i>R</i>	<i>I</i>
1	18.45 ± 0.03	16.99 ± 0.01	15.66 ± 0.02	14.85 ± 0.01	14.16 ± 0.03
2	17.49 ± 0.03	17.13 ± 0.02	16.26 ± 0.02	15.75 ± 0.01	15.27 ± 0.02
3	18.13 ± 0.04	18.24 ± 0.02	17.63 ± 0.01	17.20 ± 0.02	16.79 ± 0.02
4	18.02 ± 0.03	17.52 ± 0.02	16.61 ± 0.01	16.07 ± 0.02	15.54 ± 0.02
5	16.89 ± 0.03	16.81 ± 0.02	16.04 ± 0.01	15.56 ± 0.01	15.06 ± 0.02
6	18.79 ± 0.02	18.25 ± 0.03	17.38 ± 0.01	16.86 ± 0.01	16.38 ± 0.02
7	18.62 ± 0.04	17.76 ± 0.02	16.72 ± 0.01	16.08 ± 0.02	15.52 ± 0.02

Table A2. UV-Optical photometry of SN 2017hpa with *Swift-UVOT*.

Date (yyyy-mm-dd)	JD (2458000+)	Phase* (d)	<i>uvw1</i> (mag)	<i>u</i> (mag)	<i>b</i> (mag)	<i>v</i> (mag)
2017-10-26	53.25	-13.05	18.37±0.16	17.59±0.10	17.09±0.05	16.63±0.06
2017-10-28	54.58	-11.72	18.35±0.24	16.91±0.12	16.74±0.07	16.49±0.12
2017-10-30	56.98	-9.32	18.09±0.23	16.35±0.09	16.38±0.07	16.17±0.11
2017-11-03	60.89	-5.41	17.00±0.10	15.38±0.04	15.62±0.04	15.66±0.06
2017-11-09	67.48	1.18	16.80±0.13	15.37±0.07	15.46±0.05	15.31±0.08
2017-11-11	69.26	2.97	17.11±0.15	15.46±0.05	—	15.38±0.09
2017-11-13	71.11	4.82	17.19±0.09	15.61±0.09	15.54±0.04	15.31±0.05
2017-11-15	73.32	7.02	17.33±0.19	15.82±0.08	15.70±0.06	15.36±0.09
2017-11-17	75.18	8.88	17.86±0.25	15.95±0.08	15.80±0.06	15.39±0.05
2017-11-23	81.08	14.78	17.97±0.16	16.77±0.09	16.39±0.05	15.81±0.08
2017-11-24	82.35	16.05	18.31±0.19	16.93±0.09	16.53±0.06	15.84±0.07
2017-11-27	85.27	18.97	18.59±0.21	17.32±0.12	16.91±0.07	16.01±0.07
2017-12-01	88.86	22.56	19.36±0.56	17.46±0.16	17.21±0.10	16.20±0.10
2017-12-07	95.43	29.13	—	18.99±0.45	17.65±0.11	16.48±0.10

*Time since *B*-band maximum (JD 2458066.3).**Table A3.** Optical photometry of SN2017hpa from HCT.

Date (yyyy-mm-dd)	JD (2458000+)	Phase* (d)	<i>U</i> (mag)	<i>B</i> (mag)	<i>V</i> (mag)	<i>R</i> (mag)	<i>I</i> (mag)
2017-10-31	58.45	-7.8	15.68 ± 0.13	15.98 ± 0.03	15.95 ± 0.02	15.82 ± 0.02	15.75 ± 0.03
2017-11-01	59.43	-6.8	15.49 ± 0.15	15.77 ± 0.03	15.82 ± 0.02	15.69 ± 0.02	15.63 ± 0.02
2017-11-02	60.37	-5.9	15.37 ± 0.15	15.63 ± 0.06	15.75 ± 0.03	15.54 ± 0.03	15.52 ± 0.02
2017-11-09	67.19	0.9	15.26 ± 0.14	15.41 ± 0.02	15.39 ± 0.01	15.31 ± 0.02	15.43 ± 0.02
2017-11-10	68.21	2.0	15.36 ± 0.19	15.44 ± 0.03	15.40 ± 0.01	15.30 ± 0.01	15.45 ± 0.01
2017-11-15	73.27	7.0	15.69 ± 0.15	15.68 ± 0.03	15.39 ± 0.01	15.39 ± 0.01	15.61 ± 0.01
2017-11-19	77.43	11.1	—	16.04 ± 0.04	15.48 ± 0.01	15.63 ± 0.02	16.02 ± 0.04
2017-11-22	80.28	13.9	16.57 ± 0.09	16.36 ± 0.02	15.75 ± 0.01	15.79 ± 0.01	15.96 ± 0.02
2017-11-29	87.36	21.1	—	17.23 ± 0.02	16.26 ± 0.02	15.98 ± 0.01	15.83 ± 0.02
2017-12-17	105.24	38.9	—	18.38 ± 0.02	17.18 ± 0.02	16.74 ± 0.01	16.30 ± 0.02
2017-12-26	114.21	47.9	—	18.60 ± 0.03	17.48 ± 0.02	17.12 ± 0.01	16.76 ± 0.02
2017-12-29	117.24	50.9	—	18.62 ± 0.04	17.54 ± 0.02	17.20 ± 0.02	16.92 ± 0.02
2018-01-05	124.09	57.8	—	—	17.78 ± 0.02	17.48 ± 0.01	17.33 ± 0.03
2018-01-21	140.12	73.8	19.55 ± 0.25	19.02 ± 0.03	18.12 ± 0.03	17.94 ± 0.02	17.97 ± 0.03
2018-02-02	152.11	85.8	—	—	18.37 ± 0.02	18.25 ± 0.02	—
2018-02-03	153.14	86.9	19.95 ± 0.19	19.08 ± 0.07	18.40 ± 0.02	18.24 ± 0.03	18.26 ± 0.04
2018-02-09	159.27	93.0	—	—	18.58 ± 0.03	18.48 ± 0.02	18.63 ± 0.04

*Time since *B*-band maximum (JD 2458066.3).

Table A4. Log of spectroscopic observations of SN2017hpa from HCT.

Date (yyyy-mm-dd)	JD (2458000+)	Phase* (d)	Range (Å)
2017-10-30	57.43	-8.9	3500-7800; 5200-9100
2017-10-31	58.46	-7.8	3500-7800; 5200-9100
2017-11-01	59.47	-6.7	3500-7800
2017-11-02	60.39	-5.9	3500-7800; 5200-9100
2017-11-09	67.22	0.9	3500-7800; 5200-9100
2017-11-10	68.23	1.9	3500-7800; 5200-9100
2017-11-19	77.36	11.1	3500-7800; 5200-9100
2017-11-22	80.30	14.1	3500-7800; 5200-9100
2017-11-29	87.23	20.9	3500-7800; 5200-9100
2017-12-01	89.31	23.1	3500-7800; 5200-9100
2017-12-05	93.19	26.9	3500-7800; 5200-9100
2017-12-17	105.26	39.0	3500-7800; 5200-9100
2017-12-26	114.24	47.9	3500-7800; 5200-9100
2017-12-29	117.25	51.0	3500-7800; 5200-9100
2018-01-05	124.13	57.9	3500-7800; 5200-9100
2018-01-21	140.22	73.9	3500-7800; 5200-9100
2018-01-30	149.17	82.9	3500-7800; 5100-9100
2018-02-03	153.07	86.8	3500-7800
2018-02-09	159.14	92.8	3500-7800; 5200-9100
2018-02-13	163.13	96.8	3500-7800
2018-02-20	170.07	103.8	3500-7800
2018-02-25	175.06	108.8	3500-7800

*Time since *B*-band maximum (JD 2458066.3).**Table A5.** *syn++* fit to the pre-maximum spectra of SN 2017hpa.

Phase*: - 13.8 d v_{phot} : 15,000 km s ⁻¹ v_{max} : 30,000 km s ⁻¹ T_{BB} : 10,000 K									
Parameters	C II	Mg II	Si II _{PV}	Si II _{HV}	S II	Ca II _{PV}	Ca II _{HV}	Fe II	Fe III
log (tau)	-0.5	0.5	0.9	1.5	0.2	1.0	2.3	1.0	-0.8
v_{min} (× 10 ³) km s ⁻¹	15.0	16.0	15.0	22.0	15.0	17.0	25.0	17.0	15.0
aux (× 10 ³) km s ⁻¹	2.1	1.8	2.6	2.45	1.0	2.0	2.7	0.8	3.2
T_{exc} (× 10 ³) K	10	10	10	10	10	10	10	10	10

Phase*: - 8.9 d v_{phot} : 13,800 km s ⁻¹ v_{max} : 30,000 km s ⁻¹ T_{BB} : 11,000 K										
Parameters	C II	Mg II	Si II _{PV}	Si II _{HV}	Si III	S II	Ca II _{PV}	Ca II _{HV}	Fe II	Fe III
log (tau)	0.2	0.2	0.03	0.5	-0.6	-0.8	0.5	1.5	-0.5	-0.5
v_{min} (× 10 ³) km s ⁻¹	13.8	15.0	13.8	18.0	13.8	13.8	14.0	20.0	13.8	13.8
aux (× 10 ³) km s ⁻¹	0.4	1.7	3.5	2.5	2.5	0.8	2.0	4.0	1.0	3.0
T_{exc} (× 10 ³) K	10	10	10	10	10	10	10	10	10	10

*Time since *B*-band maximum (JD 2458066.3).**Table A6.** *TARDIS* fit to the pre-maximum spectra of SN 2017hpa.

Phase*: - 8.9 d t_{exp} *: 8.0 day v_{inner} *: 13,000 km s ⁻¹ v_{outer} : 23,000 km s ⁻¹ Luminosity (log L _⊙): 9.37						
Elements		C	O	Mg	Si	Ca
Abundances		0.03	0.26	0.10	0.53	0.08

*Time since *B*-band maximum (JD 2458066.3).

*Time since explosion (JD 2458049.41).

*velocity at the inner boundary of the photosphere.